Inorganic Chemistry
Article
pubs.acs.org/IC

# Alkaline Earth Metal Ion/Dihydroxy–Terephthalate MOFs: Structural Diversity and Unusual Luminescent Properties

Antigoni Douvali,[†] Giannis S. Papaefstathiou,[‡] Maria Pia Gullo,[§] Andrea Barbieri,[§] Athanassios C. Tsipis,[†] Christos D. Malliakas,[∥] Mercouri G. Kanatzidis,[∥] Ioannis Papadas,[⊥] Gerasimos S. Armatas,[⊥] Antonios G. Hatzidimitriou,[#] Theodore Lazarides,*[,#] and Manolis J. Manos*[,†]

[†] Department of Chemistry, University of Ioannina, 45110 Ioannina, Greece

[‡] Laboratory of Inorganic Chemistry, Department of Chemistry, National and Kapodistrian University of Athens, Panepistimiopolis, Zografou 157 71, Athens, Greece

[§] Italian National Research Council (CNR), Institute for Organic Synthesis and Photoreactivity (ISOF), Via P. Gobetti 101, 40129 Bologna, Italy

[∥] Department of Chemistry, Northwestern University, Evanston, Illinois 60208, United States

[⊥] Department of Materials Science and Technology, University of Crete, 71003 Heraklion, Greece

[#] Department of Chemistry, Aristotle University of Thessaloniki, 54124 Thessaloniki, Greece

*Supporting Information*

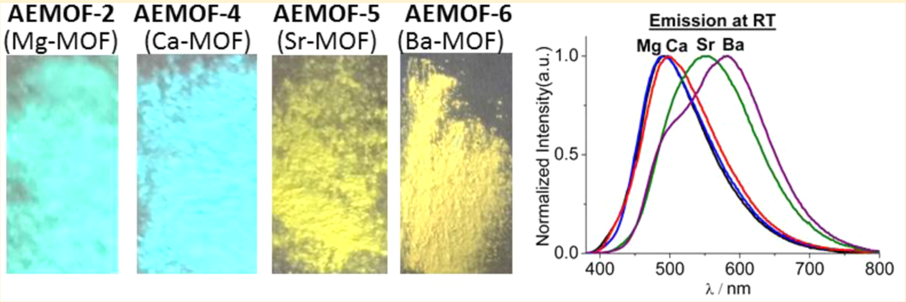

**ABSTRACT:** Alkaline earth (group 2) metal ion organic frameworks (**AEMOFs**) represent an important subcategory of MOFs with interesting structures and physical properties. Five MOFs, namely, $[Mg_2(H_2dhtp)_2(\mu\text{-}H_2O)(NMP)_4]$ (**AEMOF-2**), $[Mg_2(H_2dhtp)_{1.5}(DMAc)_4]Cl\cdot DMAc$ (**AEMOF-3**), $[Ca(H_2dhtp)(DMAc)_2]$ (**AEMOF-4**), $[Sr_3(H_2dhtp)_3(DMAc)_6]\cdot H_2O$ (**AEMOF-5**), and $[Ba(H_2dhtp)(DMAc)]$ (**AEMOF-6**) ($H_4dhtp$ = 2,5-dihydroxy-terepthalic acid; DMAc = *N*,*N*-dimethylacetamide; NMP = *N*-methylpyrrolidone), are presented herein. The reported MOFs display structural variety with diverse topologies and new structural features. Interestingly, **AEMOF-6** is the first example of a $Ba^{2+}$–$H_2dhtp^{2-}$ MOF, and **AEMOF-5** is only the second known $Sr^{2+}$–$H_2dhtp^{2-}$ MOF. Detailed photoluminescence studies revealed alkaline earth metal ion-dependent fluorescence properties of the materials, with the heavier alkaline earth metal ions exhibiting red-shifted emission with respect to the lighter ions at room temperature. A bathochromic shift of the emission was observed for the MOFs (mostly for **AEMOF-3** and **AEMOF-4**) at 77 K as a result of excited state proton transfer (ESIPT), which involves an intramolecular proton transfer from a hydroxyl to an adjacent carboxylic group of the $H_2dhtp^{2-}$ ligand. Remarkably, **AEMOF-6** displays rare yellow fluorescence at room temperature, which is attractive for solid state lighting applications. To probe whether the alkaline earth metal ions are responsible for the unusual luminescence properties of the reported MOFs, the potential energy surfaces (PESs) of the ground, $S_0$, and lowest energy excited singlet, $S_1$, states of model complexes along the intramolecular proton transfer coordinate were calculated by DFT and TD-DFT methods.

## INTRODUCTION

Metal organic frameworks (MOFs) are porous crystalline solids constructed from organic molecules (bridging ligands) acting as linkers and metal ions or clusters serving as connecting points or vise versa.[1,2] MOFs based on alkaline earth (group 2) metal ions have received much less attention compared to those of transition metal ions, with the $Sr^{2+}$ and $Ba^{2+}$ MOFs being still scarce. However, alkaline earth metal ion MOFs (**AEMOFs**) have several unique attributes such as low density, reduced toxicity, relatively low cost (because of the abundant alkaline earth metal ions), stability in air and in various solvents, etc.[3] Furthermore, some **AEMOFs** have shown quite interesting gas sorption, photochromic, and photoluminescence-sensing properties.[3]

**Received:** March 9, 2015
**Published:** June 3, 2015

ACS Publications

DOI: 10.1021/acs.inorgchem.5b00539

We have currently initiated a research program involving the synthesis and design of new highly luminescent **AEMOFs** with potential sensing properties for industrial and environmental applications. The first result of these investigations was the discovery of $[Mg(H_2dhtp)(H_2O)_2]\cdot DMAc$ (**AEMOF-1**).[4] This compound exhibits strong turquoise ligand-based emission arising from radiative deactivation of two closely lying excited states: a locally excited state and a lower lying state populated through excited state intramolecular proton transfer (ESIPT).[5] The ESIPT process involves the transfer of a proton in an electronically excited species from a hydroxyl or an amino group to a carbonyl oxygen through a pre-existing strong hydrogen bond (five- or six-membered ring configuration), Scheme 1.

**Scheme 1. Proton Transfer from Hydroxyl to Carbonyl Oxygen Atom through a Strong Hydrogen Bond (Six-Membered Ring Configuration)**

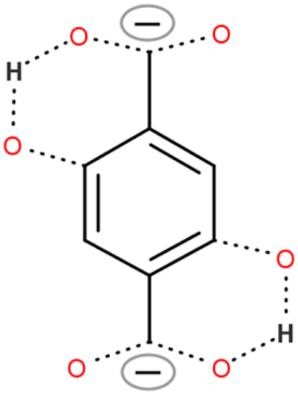

Although this phenomenon has been extensively studied in molecular systems,[5] analogous studies in MOFs are scarce.[3f,g,4] The energetics of the ESIPT process are known to be sensitive to the environment around the emitting chromophore, thus making such chromophores particularly appealing for sensing applications.[5e,f] Additionally, the large Stokes shifts associated with the ESIPT process offer the advantage of facile spectral discrimination between excitation and emission signal, thus eliminating possible errors and misinterpretations caused by the self-absorption (inner filter) effects. Furthermore, ESIPT sensors often exhibit analyte-specific shifts in emission wavelength in addition to quenching or enhancement, thereby offering the possibility of superior selectivity and direct analyte recognition.[6] Indeed, **AEMOF-1** showed extraordinary ability for detection of traces of water in various organic solvents via an unusual "turn-on" luminescence sensing mechanism that involves enhancement accompanied by a red shift in emission wavelength.[4]

Building upon our previous studies on **AEMOFs** exhibiting ESIPT luminescence, we present herein five new **AEMOFs**, namely, $[Mg_2(H_2dhtp)_2(\mu\text{-}H_2O)(NMP)_4]$ (**AEMOF-2**), $[Mg_2(H_2dhtp)_{1.5}(DMAc)_4]Cl\cdot DMAc$ (**AEMOF-3**), $[Ca(H_2dhtp)(DMAc)_2]$ (**AEMOF-4**), $[Sr_3(H_2dhtp)_3(DMAc)_6]\cdot H_2O$ (**AEMOF-5**), and $[Ba(H_2dhtp)(DMAc)]$ (**AEMOF-6**). The compounds display a noticeable structural diversity adopting 2-D (**AEMOF-3**) or 3-D frameworks (**AEMOF-2**, **AEMOF-4**, **AEMOF-5**, **AEMOF-6**) with a variety of secondary building units (SBUs) and network topologies, new $H_2dhtp^{2-}$ coordination modes, etc. It should also be noted that **AEMOF-6** represents the first example of a $Ba^{2+}$–$H_2dhtp^{2-}$ MOF. The **AEMOFs** exhibit interesting and unusual luminescent properties including a strong dependence of emission wavelength on the alkaline earth metal ion (red-shifted emission with heavier alkaline earth metal ions) and a bathochromic shift of their emission at low temperature (77 K) (particularly pronounced for **AEMOF-3** and **AEMOF-4**). The latter feature makes some members of the **AEMOF** series potentially attractive for use in temperature sensing applications.[6f] It is worth pointing out that **AEMOF-6** displays bright yellow emission (quantum yield of 34%). Yellow emitters are rarely observed among MOFs and are particularly desirable as they fill the yellow gap of primary light-emitting diode phosphors.[7] To the best of our knowledge, bright yellow emission (quantum yield of 32%) was achieved in only one MOF through partial replacement of up to 20% of $Ba^{2+}$ centers with luminescent $Eu^{2+}$ ions in the compound $[Ba(Im)_2]$ (Im = imidazole).[7] The luminescence in this example is due to 5d → 4f transitions in the $Eu^{2+}$ ions. Thus, **AEMOF-6** represents the first example of a MOF exhibiting purely ligand-based yellow luminescence with a quantum yield exceeding that of the Eu-doped barium imidazolate.

## ■ EXPERIMENTAL SECTION

**Materials.** All reagents and solvents were commercially available and used as received.

**Physical Measurements.** IR spectra were recorded on KBr pellets in the 4000–400 $cm^{-1}$ range using a PerkinElmer Spectrum GX spectrometer. Powder X-ray diffraction (PXRD) measurements were carried out on a Rigaku Ultima IV diffractometer with a Cu $K\alpha$ source. Thermogravimetric analysis (TGA) data were recorded with a PerkinElmer Pyris –Diamond TGA/DTA analyzer. UV–vis diffuse reflectance spectra were obtained at room temperature on a Shimadzu 1200 PC in the wavelength range of 200–800 nm. $BaSO_4$ powder was used as a reference (100% reflectance) and base material on which the powder sample was coated. The reflectance data were converted to absorption using the Kubelka–Munk function. $N_2$ adsorption–desorption isotherms were measured at 77 K on a Quantachrome Nova 3200*e* sorption analyzer. Before analysis, all samples were degassed at 200 °C under vacuum ($<10^{-5}$ Torr) for 12 h. The specific surface areas were calculated by applying the Brumauer–Emmett–Teller (BET) method to the adsorption isotherms in the 0.05–0.25 relative pressure ($P/P_o$) range. Samples were degassed at 200 °C for about 12 h prior to analysis. The total pore volumes were derived from the adsorbed volume at $P/P_o = 0.95$. $CO_2$ adsorption isotherms were measured at 195 K using an IGA-003 gravimetric adsorption analyzer (Hiden Isochema, U.K.). Before measurements, all samples were degassed at 200 °C under vacuum for 12 h.

**Syntheses.** *AEMOF-2*. $Mg(OAc)_2\cdot 4H_2O$ (0.08 g, 0.37 mmol) was added as a solid into a stirred solution of $H_4dhtp$ (0.12 g, 0.61 mmol) in NMP/$H_2O$ (9:1 v/v, 5 mL, pH ≈ 7.5) in a Teflon cup. The mixture was stirred for ~5 min, and then the Teflon cup was transferred into a 23 mL Teflon-lined stainless steel autoclave. The autoclave was sealed and placed in an oven operated at 120 °C, remained undisturbed at this temperature for 20 h, and then was allowed to cool at room temperature. Colorless polyhedral crystals of **AEMOF-2** were isolated by filtration and dried in the air. Yield: 0.14 g (~87%).

*AEMOF-3*. $MgCl_2$ (0.03 g, 0.32 mmol) was added as a solid into a stirred solution of $H_4dhtp$ (0.03 g, 0.15 mmol) in DMAc (3 mL) in a Teflon cup. Then, the reaction was performed similarly as in the case of **AEMOF-2** (i.e., solvothermal reaction at 120 °C for ~20 h). Colorless plate-like crystals of **AEMOF-3** were isolated by filtration and dried in the air. Yield: 0.05 g (~61%, calculated for the anhydrous MOF).

*AEMOF-4*. $Ca(NO_3)_2\cdot 4H_2O$ (0.08.g, 0.34 mmol) was added as a solid into a stirred solution of $H_4dhtp$ (0.05 g, 0.25 mmol) in DMAc/$H_2O$ (9:1 v/v, 5 mL, pH ≈ 7.5) in a Teflon cup. Then, the procedure followed was identical to that for the synthesis of **AEMOF-2**. Rod-like colorless crystals of **AEMOF-4** were isolated by filtration and dried in the air. Yield: 0.09 g (~88%).

*AEMOF-5*. $Sr(NO_3)_2$ (0.03 g, 0.14 mmol) was added as a solid into a stirred solution of $H_4dhtp$ (0.05 g, 0.25 mmol) in DMAc/$H_2O$ (9:1 v/v,

Table 1. Selected Crystal Data for AEMOF-2-6

| compound | **AEMOF-2** | **AEMOF-3** | **AEMOF-4** | **AEMOF-5** | **AEMOF-6** |
|---|---|---|---|---|---|
| chemical formula | $C_{36}H_{46}Mg_2N_4O_{17}$ | $C_{32}H_{51}ClMg_2N_5O_{14}$ | $C_{16}H_{22}CaN_2O_8$ | $C_{48}H_{68}N_6O_{25}Sr_3$ | $C_{12}H_{13}BaNO_7$ |
| formula mass | 855.39 | 813.85 | 410.44 | 1391.94 | 420.57 |
| cryst syst | monoclinic | monoclinic | monoclinic | triclinic | monoclinic |
| $a$ (Å) | 11.993(2) | 11.413(2) | 18.659(4) | 11.439(5) | 28.110(2) |
| $b$ (Å) | 19.632(4) | 29.479(6) | 11.251(2) | 11.966(5) | 11.6839(9) |
| $c$ (Å) | 18.143(4) | 12.376(3) | 10.015(2) | 12.113(5) | 8.6676(6) |
| $\alpha$ (deg) | 90.00 | 90.00 | 90.00 | 101.036(5) | 90.00 |
| $\beta$ (deg) | 102.06(3) | 94.95(3) | 114.12(3) | 106.890(5) | 98.795(2) |
| $\gamma$ (deg) | 90.00 | 90.00 | 90.00 | 107.950(5) | 90.00 |
| unit cell vol. (Å$^3$) | 4177.3(14) | 4148.4(14) | 1918.9(7) | 1435.6(11) | 2813.3(4) |
| temp. (K) | 293(2) | 293(2) | 298(2) | 293(2) | 298(2) |
| space group | $C2/c$ | $P2_1/n$ | $C2/c$ | $P\bar{1}$ | $C2/c$ |
| $Z$ | 4 | 4 | 4 | 1 | 8 |
| no. reflns measd | 18 421 | 20 202 | 18 661 | 25 944 | 40 136 |
| no. independent reflns | 3678 | 7293 | 2798 | 7397 | 6677 |
| $R_{int}$ | 0.0633 | 0.0714 | 0.0363 | 0.0235 | 0.0333 |
| $R_1{}^a$ values ($I > 2\sigma(I)$) | 0.0692 | 0.0964 | 0.0397 | 0.0368 | 0.0281 |
| $wR(F^2)^b$ values ($I > 2\sigma(I)$) | 0.1582 | 0.2683 | 0.1200 | 0.1102 | 0.0635 |

$^aR_1 = \Sigma||F_o| - |F_c||/\Sigma|F_o|$. $^bwR(F^2) = [\Sigma[w(F_o{}^2 - F_c{}^2)^2]/\Sigma[wF_o{}^2)^2]]^{1/2}$, $w = 1/[\sigma^2(F_o{}^2) + (m{\cdot}p)^2 + n{\cdot}p]$, $p = [\max(F_o{}^2,0) + 2F_c{}^2]/3$, and $m$ and $n$ are constants.

5 mL, pH ≈ 7.5) in a Teflon cup. Then, the reaction was performed similarly as in the case of **AEMOF-2**. Rod-like colorless crystals of **AEMOF-5** were isolated by filtration and dried in the air. Yield: 0.06 g (~86%).

*AEMOF-6*. $Ba(NO_3)_2$ (0.04 g, 0.15 mmol) was added as a solid into a stirred solution of $H_4$dhtp (0.05 g, 0.25 mmol) in DMAc/$H_2O$ (9:1 v/v, 5 mL, pH ≈ 7.5) in a Teflon cup. The solvothermal reaction procedure followed for the other MOFs has been also applied in the case of **AEMOF-6**. Needle-like crystals of **AEMOF-6** were isolated by filtration and dried in the air. Yield: 0.06 g (~93%).

The purity of all products was confirmed by comparison of the experimental PXRD patterns to those calculated from the single-crystal X-ray data (see Figures S1−S5, Supporting Information). In addition, the compounds were characterized with thermogravimetric analysis (TGA) (Figure S6−S10, Supporting Information), variable-temperature (VT) PXRD (Figure S11−S15, Supporting Information), infrared spectroscopy (Figure S16, Supporting Information), and gas sorption measurements (Figure S17−S20, Supporting Information).

**Single-Crystal X-ray Crystallography.** Data collection was carried out with STOE imaging plate diffraction system (IPDS-2) (for **AEMOF-2**) or Bruker Apex-II CCD (for **AEMOF-3−6**) using graphite-monochromatized Mo K$\alpha$ radiation. The data were collected at room temperature over a full sphere of reciprocal space. Cell refinement, data reduction, and numerical absorption correction were carried out using X-AREA suite or Bruker SAINT software package.[8a] The intensities were extracted by the program XPREP.[8b] The structures were solved with direct methods using SHELXS, and least-squares refinement was done against $F_{obs}{}^2$ using routines from the SHELXTL software.[8b] In order to limit the disorder of the solvent molecules in the structures of the compounds, various restraints (ISOR, DELU, SIMU) have been applied in the refinement.

CCDC 1042418−1042422 contain the supplementary crystallographic data for this paper. These data can be obtained free of charge via www.ccdc.cam.ac.uk/data_request/cif. Selected crystal data for all compounds are given in Table 1.

**Photoluminescence Measurements.** All determinations made use of powder samples placed inside two quartz slides. Absolute photoluminescence quantum yields were measured according to the method of deMello[9a] by using an integrating sphere and placed inside an Edinburgh FLS 920 fluorimeter.[9b] All measurements were repeated three times. The limit of detection of the system is 2%. Luminescence lifetimes were measured with an IBH 5000F time-correlated single-photon counting apparatus by using a pulsed NanoLED excitation source at 331 nm. Analysis of the luminescence decay profiles against time was accomplished with the decay analysis software DAS6 provided by the manufacturer, with an estimated error in the lifetimes of 10%. Lifetime measurements were repeated 3−5 times.

**Computational Details.** All calculations were performed using the Gaussian09 program suite.[10] The geometries of all stationary points were fully optimized, without symmetry constraints, employing the 1997 hybrid functional of Perdew, Burke, and Ernzerhof[11] as implemented in the Gaussian09 program suite.[10] This functional uses 25% exchange and 75% correlation weighting and is denoted as PBE0. For the geometry optimizations we used the Def2-TZVP basis set[12] for all atoms in the (htp)M$^+$ (htp$^-$ = 2-hydroterephthalate ligand; M = Mg, Ca) model complexes. However, for (htp)Sr$^+$, due to convergence problems in the optimization of the excited $S_1$ state we used the hdf-TZVP basis set[12] for all atoms, and for (htp)Sr$^+$ we used the DZP basis set for Ba and the hdf-TZVP basis set[12] for the nonmetal atoms. The potential energy surfaces (PESs) of the ground state ($S_0$) and the lowest energy excited singlet state ($S_1$) of the model complexes along the proton transfer coordinate in the gas phase were calculated at the same level of theory. The natural bond orbital (NBO) population analysis was performed using Weinhold's methodology as implemented in the NBO 6.0 software.[13] Magnetic shielding tensors have been computed with the GIAO (gauge-including atomic orbitals) DFT method[14] as implemented in the Gaussian09 series of programs[10] employing the PBE0 functional. Nucleus-independent chemical shift (NICS) values were computed at the same level according to the procedure described by Schleyer et al.[15] Absorption and emission spectra were simulated in the gas phase by TD-DFT calculations at the PBE0/Def2-TZVP and PBE0/hdf-TZVP levels, including the lowest 20 singlet−singlet excitations.

## ■ RESULTS AND DISCUSSION

**Synthesis.** As mentioned in the Introduction, we recently initiated a research program aiming at the synthesis of new alkaline earth metal ion MOFs with ESIPT-based luminescence for potential applications as sensors.[4] We selected $H_4$dhtp as a suitable polytopic (polydentic) ligand to synthesize such MOFs since this organic molecule is expected to favor the ESIPT phenomenon via a proton transfer from the hydroxyl to the carboxylic oxygen atoms in the excited state (Scheme 1).[3f,g,4] Of course, this ligand should be in its dianionic form $H_2$dhtp$^{2-}$ (i.e., the OH groups should not be be deprotonated) in the MOFs to result in compounds with ESIPT-based luminescence, and therefore, the use of base should be avoided for successful preparation of such materials.

In a previous communication, we reported the compound $[Mg(H_2dhtp)(H_2O)_2]\cdot DMAc$ (**AEMOF-1**), which was prepared by the reaction of $Mg(OAc)_2\cdot 4H_2O$ and $H_4dhtp$ in $DMAc/H_2O$ (9:1 v/v) at 120 °C.[4] Varying the synthesis conditions (solvent, metal source, etc.), we now achieved isolation of additional $Mg^{2+}$–$H_2dhtp^{2-}$ phases. Thus, reaction of $Mg(OAc)_2\cdot 4H_2O$ and $H_4dhtp$ in a molar ratio 1:1.7 in NMP/$H_2O$ (9:1) at 120 °C afforded compound **AEMOF-2** in ~87% yield. Note that the same reaction with a molar ratio 1:1 resulted in a mixture of CPO-27-Mg[3e] and **AEMOF-2**. In addition, the reaction of $MgCl_2$ and $H_4dhtp$ in a molar ratio 2:1 in DMAc led to compound **AEMOF-3** in ~61% yield.

It was also possible to prepare $Ca^{2+}$, $Sr^{2+}$, and $Ba^{2+}$/$H_2dhtp^{2-}$ MOFs (**AEMOF-4–6**) in high yields (>85%) by reacting $H_4dhtp$ with the corresponding alkaline earth metal ion nitrate salts in $DMAc/H_2O$ (9:1 v/v) at 120 °C. We should note that the addition of water in the reaction mixture was necessary for the isolation of **AEMOF-4** and **AEMOF-6**, although determination of their crystal structures did not reveal existence of water as ligand or lattice solvent (see below). The synthetic procedures yielding compounds **AEMOF-2–6** are summarized in Scheme 2.

**Scheme 2. Synthetic Routes Leading to Compounds AEMOF-2–6**

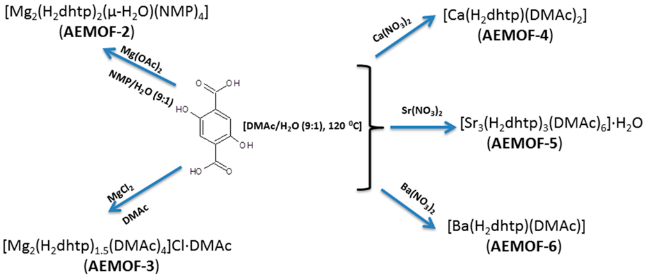

**Crystal Structure of AEMOF-2.** Representation of the secondary building unit (SBU)/3-D structure and net topology of **AEMOF-2** are shown in Figure 1. Compound **AEMOF-2** is a 3-D coordination polymer that crystallizes in the monoclinic space group *C*2/*c*. Its SBU consists of a dinuclear $[Mg_2(COO)_4(\mu_2\text{-}H_2O)(NMP)_4]$ unit in which each $Mg^{2+}$ ion is coordinated in octahedral geometry by two $\eta^1{:}\eta^1{:}\mu_2\text{-}COO^-$ and one monodentate $COO^-$ groups, one $\mu_2\text{-}OH_2$, and two terminal NMP ligands (Figure 1A). The second (noncoordinated) O atom of the monodentate $COO^-$ moiety forms an intradimer H bond (~2.7 Å) with the $\mu_2\text{-}OH_2$ molecule. The hydroxyl groups are also involved in H bonds (~2.5–2.6 Å) with the carbonyl oxygen atoms of the $H_2dhtp^{2-}$ ligands. The dinuclear units are interconnected through the $H_2dhtp^{2-}$ ligands, creating a three-dimensional framework with the terminal NMP ligands situated inside the cavities (Figure 1B). If NMP ligands were ignored then the void volume of **AEMOF-2** calculated by MERCURY[16] would be ~58% of the unit cell volume.

Considering that the structure consists of isolated $[Mg_2]$ dimers bridged by terephthalates, each $[Mg_2]$ serves as a 4-coordinated node and the underlying network is **dia** with point symbol $6^6$. Alternatively, if we adopt the simplification method of M. O'Keeffe and O. M. Yaghi[17] and consider the carboxylate C atoms as the connecting points then the network consists of linked distorted supertetrahedra with a three letter code **dia-a** and point symbol $3^6.12^3$ (Figure 1C).

**Crystal Structure of AEMOF-3.** Compound **AEMOF-3** displays a 2-D framework and crystallizes in the monoclinic $P2_1/n$ space group. The SBU, 2-D structure, and network topology are shown in Figure 2.

The structure of **AEMOF-3** is based on a cationic dinuclear SBU $[Mg_2(COO)_3(DMAc)_4]^+$ in which there are two crystallographicaly unique $Mg^{2+}$ (Mg1 and Mg2) both octahedrally coordinated with carboxylate groups from two types of $H_2dhtp^{2-}$ ligands (A and B), Figure 2A. Besides the ligation of both $Mg^{2+}$ with two $\eta^1{:}\eta^1{:}\mu_2\text{-}COO^-$ (from $H_2dhtp^{2-}$ ligands of type A) and four DMAc terminal ligands (two for each $Mg^{2+}$), there are significant differences in the coordination environment of the two $Mg^{2+}$ ions. Thus, the coordination environment of Mg1 is completed by two carboxylate O atoms from one $H_2dhtp^{2-}$ ligand of type B (showing the coordination mode $\eta^1{:}\eta^2{:}\mu_2\text{-}COO^-$), whereas the octahedral coordination sphere of Mg2 is filled by one OH and one carboxylate oxygen atom from the $H_2dhtp^{2-}$ ligand of type B. The $[Mg_2]$ SBUs are interconnected to form a layered structure with open windows (Figure 2B), which host guest DMAc molecules (Figure S21, Supporting Information). The cationic layers are arranged parallel to each other, while the $Cl^-$ anions balancing the charge of the layers are found in the interlayer space and form H bonds (~2.95 Å) with the OH groups of $H_2dhtp^{2-}$ ligands of type B (Figure S21, Supporting Information).

The 2-D framework of **AEMOF-3** displays a herringbone (**hsb**) topology which is a Shubnikov hexagonal plane net with point symbol $6^3$, with each $[Mg_2]$ serving as a 3-coordinated T-shaped node (Figure 2C).

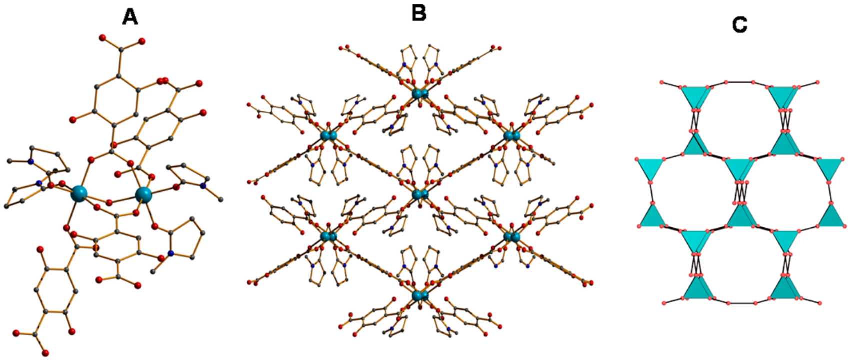

**Figure 1.** (a) SBU, (b) 3-D structure, and (c) **dia** net of **AEMOF-2** viewed down the *a* axis. H atoms were omitted for clarity. Color code: Mg, turquoise; C, gray; O, red; N, blue.

DOI: 10.1021/acs.inorgchem.5b00539
*Inorg. Chem.* 2015, 54, 5813–5826

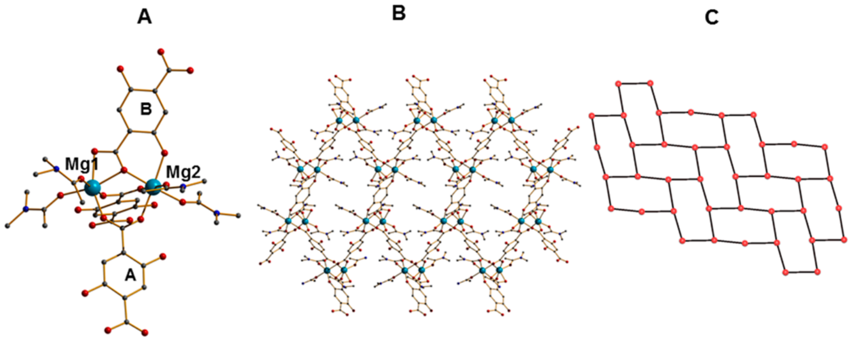

**Figure 2.** Representation of (a) SBU, (b) 2-D structure viewed down the *c* axis, and (c) **hsb** net of **AEMOF-3**. H atoms, $Cl^-$ anions, and guest DMAc molecules were omitted for clarity. Color code: Mg, turquoise; C, gray; O, red; N, blue.

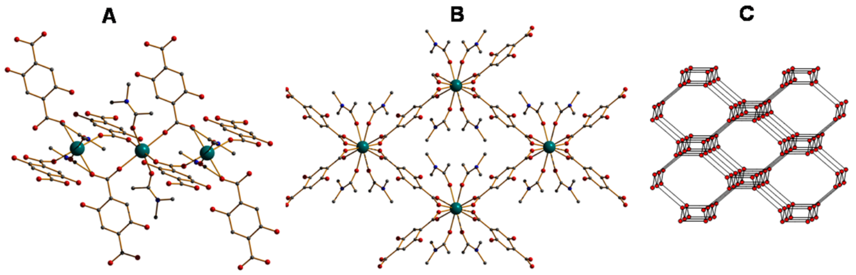

**Figure 3.** Representation of the (a) chain of $CaO_6$ octahedra, (b) 3-D structure viewed down the *c* axis, and (c) **sra** net of **AEMOF-4**. H atoms were omitted for clarity. Color code: Ca, blue-green; C, gray; O, red; N, blue.

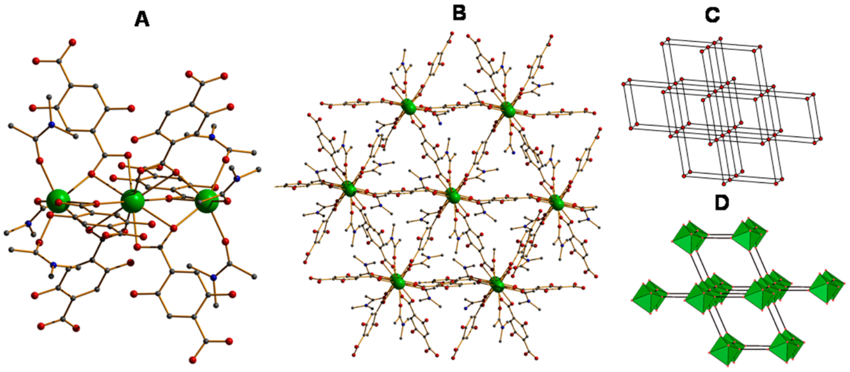

**Figure 4.** Representation of the (a) trinuclear SBU, (b) 3-D structure, (c) **pcu** net of **AEMOF-5**, and (d) alternative topological description of **AEMOF-5** as a **pcu-a** net. H atoms were omitted for clarity. Color code: Sr, green; C, gray; O, red; N, blue.

**Crystal Structure of AEMOF-4.** The compound crystallizes in the monoclinic space group *C*2/*c*. There is one crystallographically unique $Ca^{2+}$ in the structure, which adopts octahedral coordination geometry and is linked to four carboxylate oxygen atoms from different $H_2dhtp^{2-}$ ligands and two terminal DMAc ligands in trans configuration. Each $Ca^{2+}$ ion is connected to two neighboring $Ca^{2+}$ by four $\eta^1$:$\eta^1$:$\mu_2$-$COO^-$ groups forming a chain (rod) of linked $CaO_6$ octahedra running parallel to the *c* axis (Figure 3A). The chains are interconnected through the $H_2dhtp^{2-}$ linkers to form a 3-D framework (Figure 3B) with the DMAc terminal ligands filling the pore space. If DMAc molecules were removed from the structure then the void volume of **AEMOF-4** calculated by MERCURY[16] would be ~56% of the unit cell volume.

If we consider the carboxylate C atoms as the points of connection, a ladder forms along the rod of the $CaO_6$ octahedra. The ladders are further linked by the phenyl groups of the terephthalates to form a uninodal 4-coordinated network (Figure 3C). The three letter code of this net is **sra** with point symbol $4^2.6^3.8$ and is exactly the same with those found in MOF-69, MOF-71, and MIL47/MIL53/MIL60.[17] Comparing the topological features of this net with those found in **AEMOF-1**,[4] we notice that the orientation of the terminal ligands (*cis*-$H_2O$ in **AEMOF-1** versus *trans*-DMAc in **AEMOF-4**) on the $MO_6$ octahedra affects the type of the ladder created by the connection points (twisted ladder vs ladder) and consequently the underlined topology of the frameworks (i.e., **irl** in **AEMOF-1** versus **sra** in **AEMOF-4**).

**Crystal Structure of AEMOF-5.** Compound **AEMOF-5** crystallizes in the triclinic space group $P\bar{1}$ and displays a 3-D framework. The structure is based on a linear trinuclear SBU $[Sr_3(COO)_6(DMAc)_6]$, which consists of two symmetry-related $Sr^{2+}$ ions located at the corners and one central $Sr^{2+}$ ion as well as six $\eta^1$:$\eta^2$:$\mu_2$-$COO^-$ (from different $H_2dhtp^{2-}$ ligands) and six terminal DMAc ligands (Figure 4A).

The central $Sr^{2+}$ ion is 10 coordinated, and its coordination sphere contains only carboxylate oxygen atoms, whereas the corner $Sr^{2+}$ ions are 7 coordinated, and each of them is ligated with 4 carboxylate oxygen atoms and 3 terminal DMAc ligands. Each [$Sr_3$] is linked to 6 neighboring [$Sr_3$] clusters by the $H_2dhtp^{2-}$ ligands, and thus, a 3D framework (Figure 4B) with a **pcu** topology (Figure 4C) and point symbol $4^{12}.6^3$ is formed. If we, alternatively, consider that the carboxylate C atoms form a superoctahedron then a 5-coordinated network forms. The underlying topology of the latter net conforms to **cab** (**pcu-a**) with point symbol $3^4.4^2.8^4$ (Figure 4D). The terminal DMAc ligands are directed toward the cavities of **AEMOF-5** and fill the pore space of the structure. Ignoring them, the void volume of **AEMOF-5** calculated by MERCURY[10] would be ~55% of the unit cell volume.

**Crystal Structure of AEMOF-6.** Compound **AEMOF-6** crystallizes in the monoclinic space group *C*2/*c* and contains one crystallographically unique $Ba^{2+}$, which is nine coordinated by six carboxylate O atoms and two hydroxyl groups from the $H_2dhtp^{2-}$ ligands and one terminal (highly disordered) DMAc solvent (Figure 5A).

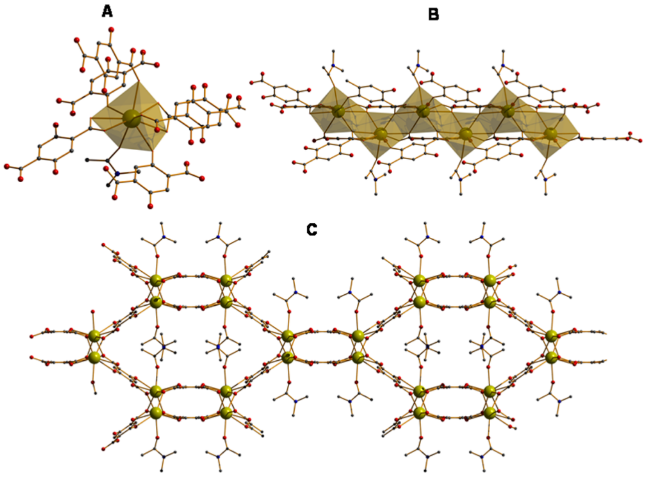

**Figure 5.** Representation of the (a) coordination environment of $Ba^{2+}$ ions, (b) rod of edge-sharing $BaO_9$, and (c) 3-D structure of **AEMOF-6** viewed down the *c* axis. H atoms were omitted for clarity. Color code: Ba, olive-green; C, gray; O, red; N, blue.

Each Ba atom is connected to 2 neighboring Ba atoms by 4 $\eta^1$:$\eta^2$:$\mu_2$-$COO^-$ forming rods of edge-sharing $BaO_9$ polyhedra (Figure 5B). Each rod is linked by $H_2dhtp^{2-}$ to three other rods, thus generating a 3-D structure with the terminal DMAc ligands situated inside the cavities (Figure 5C). If the DMAc ligands were ignored then the void volume calculated by MERCURY[16] would be 42% of the unit cell volume. Note that **AEMOF-6** is the first example of a $Ba^{2+}$ MOF with the $H_2dhtp^{2-}$ ligand (see below the comparison of **AEMOF-2–6** with reported **AEMOFs**).

By considering both the ligand and the $Ba^{2+}$ atoms as vertices, a 6-coordinated net will result. However, we cannot adopt this simplification method because the underlying net does not contain any links along the rod, and it is hard to justify finding a point on the linker as a 6-coordinated vertex. Therefore, we followed a simplification method similar to that adopted by M. O'Keeffe and O. M. Yaghi to simplify MOF-74.[17] Accordingly, vertices are placed in the center of a group of three $BaO_9$ within a rod, linked by one side of the ligand (large blue spheres on Figure S22, Supporting Information), and a single edge links these vertices to one on an adjacent rod. The resulting net is a uninodal 4-c with symbol **sra** and point symbol $4^2.6^3.8$ (Figure 6).

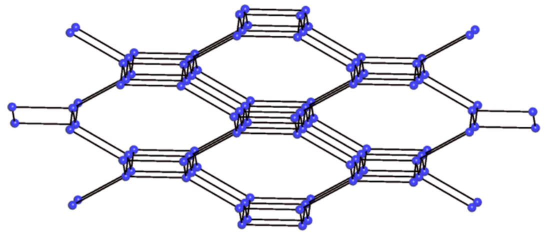

**Figure 6.** Representation of the **sra** net of **AEMOF-6**.

**Comparison of AEMOF-2 - AEMOF-6 with Reported Alkaline Earth Metal Ion –$H_2dhtp^{2-}$ MOFs.** At this point, it is worth comparing the structures of **AEMOF-2–6** with those of other alkaline earth metal ion–$H_2dhtp^{2-}$ MOFs published in the literature. In fact, only 10 **AEMOFs** with $H_2dhtp^{2-}$ have been reported so far, and remarkably, no $Ba^{2+}$–$H_2dhtp^{2-}$ MOF was known prior this work.[3e,g,4,18−20] The coordination modes of the $H_2dhtp^{2-}$ ligand in the alkaline earth metal ion MOFs (including the MOFs described in the present work) and selected structural data for these MOFs are provided in Scheme 3 and Table 2, respectively.

**Scheme 3. Coordination Modes of $H_2dhtp^{2-}$ in (known and presented here) AEMOFs**

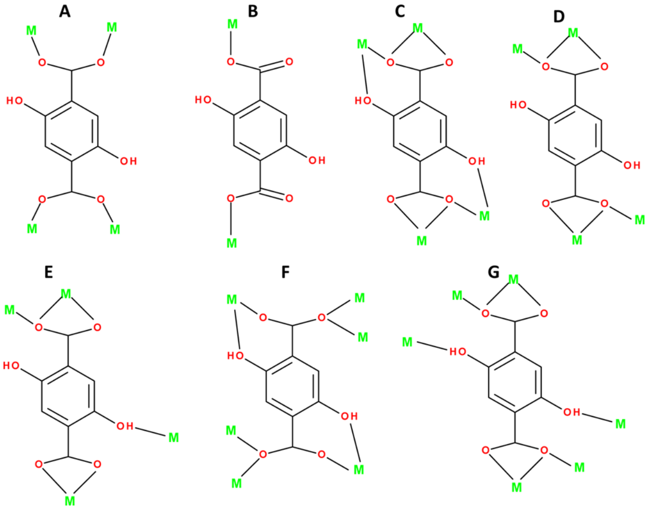

The comparison revealed that some of the coordination modes of $H_2dhtp^{2-}$ in **AEMOF-2–6** (**AEMOF-2**, A and B; **AEMOF-3**, A and C; **AEMOF-4**, A; **AEMOF-5**, D; **AEMOF-6**, G), namely, coordination modes C and D, are new in alkaline earth metal ion–$H_2dhtp^{2-}$ MOFs. Furthermore, the SBUs found in **AEMOF-2** (dinuclear [$Mg_2(COO)_4(\mu\text{-}H_2O)$]) and **AEMOF-3** (dinuclear [$Mg_2(COO)_3$]$^+$) are observed for first time in this subcategory of MOFs. The trinuclear SBU found in **AEMOF-5** ([$Sr_3(COO)_6$]) is also uncommon among the alkaline earth–$H_2dhtp^{2-}$ MOFs (only [$Mg_3(H_2dhtp)_3(DMF)_6$]·$0.75H_2O$[18] contains similar SBU). Additionally, **AEMOF-3** is the only example of alkaline earth metal ion–$H_2dhtp^{2-}$ MOF with a 2-D structure (all other examples display 3D frameworks). Finally, comparing the topological features of **AEMOF-2–6** with those of known alkaline earth–$H_2dhtp^{2-}$ MOFs it was realized that **AEMOFs-2,3** display network topologies not shown by other **AEMOFs**, whereas **AEMOF-5** adopts the same topology with the compound [$Mg_3(H_2dhtp)_3(DMF)_6$]·$0.75H_2O$,[18] and **AEMOF-4,6** adopt the same topology with [$Mg(H_2dhtp)$-

Table 2. Selected Structural Data for $AE^{2+}-H_2dhtp^{2-}$ Compounds from the Literature and the Present Work

| compound | dimensionality | $H_2dhtp^{2-}$ coordination mode | net | ref |
|---|---|---|---|---|
| $[Mg(H_2dhtp)(H_2O)_2]$ | 3-D | A | N/A | 3e |
| $[Mg(H_2dhtp)(DMF)_2]$ | 3-D | A | $\{4^2.8^4\}$(**sra**) | 3g |
| $[Mg_3(H_2dhtp)_3(DMF)_6]\cdot 0.75H_2O$ | 3-D | A | **pcu** | 18 |
| $[Mg(H_2dhtp)(H_2O)_2]\cdot$DMAc | 3-D | A | $\{4^2.6^3.8\}$(**irl**) | 4 |
| $[Mg_2(H_2dhtp)_2(\mu\text{-}H_2O)(NMP)_4]$ | 3-D | A and B | $\{3^6.12^3\}$(**dia-a**) | this work |
| $[Mg_2(H_2dhtp)_{1.5}(DMAc)_4]Cl\cdot$DMAc | 2-D | A and C | $6^3$ (**hsb**) | this work |
| $[Ca_2(H_2dhtp)_2(DMF)_2]$ | 3-D | A and G | $\{4^2.8^4\}\{4^6.6^6.8^3\}\{4^8.6^2\}_2$ | 19 |
| $[Ca(H_2dhtp)(DMF)_2]$ | 3-D | A | $\{4^2.8^4\}$(**pts**) | 19 |
| $[Ca_2(H_2dhtp)_2(H_2O)_4]$ | 3-D | B and F | $\{4^3.6^3\}_2\{4^6.6^6.8^3\}$(**fsh**) | 19 |
| $[Ca(H_2dhtp)(H_2O)_2]$ | 3-D | E | N/A | 20 |
| $[Ca(H_2dhtp)]$ | 3-D | G | N/A | 20 |
| $[Ca(H_2dhtp)(DMAc)_2]$ | 3-D | A | $\{4^2.6^3.8\}$ (**sra**) | this work |
| $[Sr(H_2dhtp)(H_2O)]$ | 3-D | G | N/A | 20 |
| $[Sr_3(H_2dhtp)_3(DMAc)_6]\cdot H_2O$ | 3-D | D | $\{3^4.4^2.8^4\}$ (**cab**) | this work |
| $[Ba(H_2dhtp)(DMAc)]$ | 3-D | G | $\{4^2.6^3.8\}$ (**sra**) | this work |

$(DMF)_2]$ (the latter adopts the **sra** topology but has mistakenly reported as **lvt**).[3g,18]

**Photophysical Studies.** As seen in Figure 7, illumination with a laboratory UV lamp (ca. 360 nm) results in bright emission from **AEMOFs** with colors ranging from different shades of turquoise (**AEMOF-2**, **-3**, and **-4**) to yellow-green or yellow (**AEMOF-5** and **-6**). This prompted us to carry out detailed photophysical studies on the series in an effort to elucidate the origin of such a pronounced color shift. The **AEMOFs** were studied in the solid state, as microcrystalline powders, by diffuse reflectance UV−vis and steady state and time-resolved fluorescence spectroscopy. Spectroscopic results are summarized in Table 3, while spectra are shown in Figures 8 and 9.

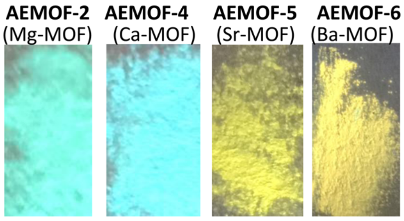

**Figure 7.** Observed emission of crystals of **AEMOF-2**, **-4**, **-5**, and **-6** compounds crushed on a filter paper and irradiated with a standard laboratory UV lamp ($\lambda_{exc}$ = 360 nm).

The diffuse reflectance spectra (Figure 8) are dominated by a broad band between ca. 250 and 425 nm maximizing at ca. 373 nm for **AEMOF-3−6** and at ca. 390 nm for **AEMOF-2**. These absorption signals are attributed to the first singlet $\pi-\pi^*$ transition of the bridging ligand (formation of the $S_1$ excited state), and the similarity in absorption profiles among the **AEMOFs** shows that the ground state of the $H_2dhtp^{2-}$ ligand is little affected by its coordination to different alkaline earth metal ions.[4]

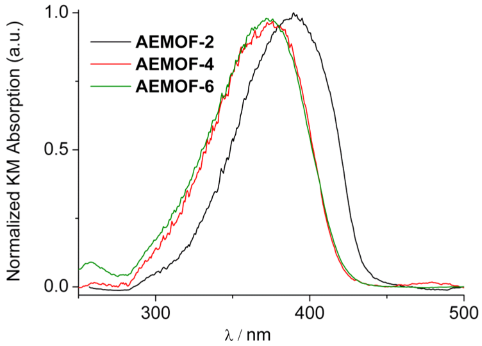

**Figure 8.** Diffuse reflectance spectra of **AEMOFs-2**, **-4** and **-6**. Spectra of **AEMOFs-3** and **-5** are essentially identical to those of **AEMOFs-4** and **-6**.

Table 3. Photophysical Data of the AEMOFs Discussed in This Paper

| compound | $\lambda_{abs}$ (nm) | $\lambda_{em}$ (298 K)[a] (nm) | $\Phi_F$ (298 K)[a] | $\tau_F$ (298 K)[b] (ns) | $\lambda_{em}$ (77 K)[a] (nm) | $\tau_F$ (77 K)[b] (ns) |
|---|---|---|---|---|---|---|
| **AEMOF-2** | 390 | 490 | 0.54 ± 0.01 | 9.1 | 496 | 10.1 |
| **AEMOF-3** | 373 | 490 | 0.54 ± 0.01 | 8.4 | 527 | 9.6 |
| **AEMOF-4** | 373 | 498 | 0.48 ± 0.01 | 8.6 | 546 | 9.3 |
| **AEMOF-5** | 373 | 552 | 0.26 ± 0.01 | 6.5 | 568 | 8.5 |
| **AEMOF-6** | 373 | 580 | 0.34 ± 0.01 | 5.7,[c] 6.9[d] | 585 | 8.0 |

[a] $\lambda_{exc}$ = 350 nm. [b] $\lambda_{exc}$ = 373 nm. [c] Monitored at 470 nm. [d] Monitored at 550 nm.

However, the fluorescence spectra (Figure 9) reveal considerable differences in the excited state properties among the members of the **AEMOF** series. At room temperature, the $Mg^{2+}$ compounds **AEMOF-2** and **AEMOF-3** show broad fluorescence bands which maximize at ca. 490 nm. Both compounds have high fluorescence quantum yields of $\Phi_F$ = 0.54 ± 0.01, and their emission signals show single-exponential decays with time constants of $\tau$ = 9.1 and 8.4 ns for **AEMOF-2** and **AEMOF-3**, respectively. At 77 K, the fluorescence signal of **AEMOF-2** remains largely unchanged with only a slight shift of about 6 nm toward lower energies. In contrast, the fluorescence spectrum of **AEMOF-3** shows a pronounced red shift in the emission maximum by ca. 37 nm (from 490 to 527 nm) upon lowering the temperature from 298 to 77 K. This temperature-induced red shift in the fluorescence maximum is in agreement to our previous observations on **AEMOF-1**, a related $Mg^{2+}$-based MOF with $H_2dhtp^{2-}$ as bridging ligand.[4]

The $Ca^{2+}$-, $Sr^{2+}$-, and $Ba^{2+}$-based **AEMOF-4**, **-5**, and **-6**, respectively, show room-temperature fluorescence that is shifted toward the infrared in comparison to their $Mg^{2+}$ counterparts. We observe that this bathochromic shift becomes more pronounced as the weight of the alkaline earth metal ion

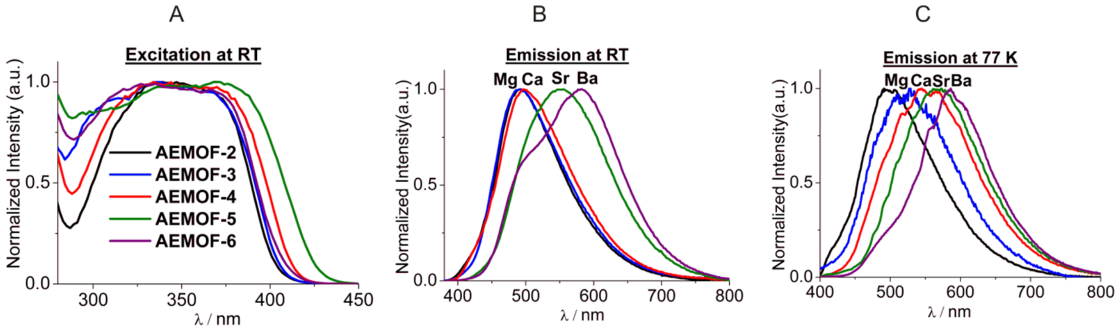

**Figure 9.** Room-temperature (~298 K) excitation (A) and emission (B) spectra of **AEMOFs-2−6**, and emission spectra of these materials at 77 K (C).

increases. Thus, upon excitation at 350 nm, **AEMOF-4** displays an intense turquoise fluorescence ($\Phi_F$ = 0.48 ± 0.01) with maximum at ca. 498 nm, while **AEMOF-5** and **-6** show yellow-green to yellow emissions with maxima at ca. 552 and 580 nm and quantum yields of $\Phi_F$ = 0.26 ± 0.01 and 0.34 ± 0.01, respectively. It is worth noting that the $Ba^{2+}$-based **AEMOF-6**, in contrast to the other members of the series, shows structured emission at room temperature with a shoulder at ca. 502 nm in addition to the maximum at 580 nm. Furthermore, the emission profile of **AEMOF-6** shows weak dependence on excitation wavelength as a slight enhancement of its high-energy component is observed upon excitation at 300 nm in comparison to the spectrum obtained upon excitation at 350 nm (Figure S23, Supporting Information). This is reflected in the excitation spectra of **AEMOF-6**, where we observe a small relative enhancement of the high-energy side of the ligand-based $\pi-\pi^*$ absorption feature when we monitor at 500 nm (Figure S24, Supporting Information). Moreover, time-resolved emission measurements on **AEMOF-6** reveal two different fluorescence lifetimes depending on monitoring wavelength. Specifically, when we monitor at 470 nm we obtain a lifetime of $\tau$ = 5.7 ns, and when we monitor at 550 nm the signal decay fits best to a time constant of $\tau$ = 6.9 ns. **AEMOF-4** and **-5** show largely featureless broad band emissions at room temperature with monoexponential decays which fit to lifetimes of $\tau$ = 8.6 and 6.5 ns, respectively. At 77 K the emission behavior of **AEMOF-4** is similar to that of **AEMOF-3** as a red shift of ca. 48 nm in the emission maximum is observed in comparison to the room-temperature spectrum (from ca. 498 to 546 nm) accompanied by a small increase in fluorescence lifetime (from $\tau$ = 8.6 to 9.3 ns). In the case of **AEMOF-5**, lowering the temperature to 77 K results in a smaller red shift of ca. 16 nm (from ca. 552 to 568 nm) in the emission maximum with a concomitant substantial 32% increase in fluorescence lifetime (from $\tau$ = 6.5 to 8.5 ns), indicating considerable vibrational deactivation at room temperature. **AEMOF-6** shows a rather modest red shift of about 5 nm in emission maximum at 77 K accompanied by loss of the shoulder, which was observed at the high-energy side (ca. 500 nm) of its room-temperature fluorescence spectrum. In addition, the emission signal of **AEMOF-6** at 77 K shows monoexponential decay with a time constant of $\tau$ = 8.0 ns independent of monitoring wavelength.

The observed temperature induced red shifts in the luminescence spectra of the **AEMOF** series is different to what is expected in solid state emission spectra where luminescence profiles normally show higher vibrational resolution and modest blue shifts at low temperatures. Note that the significant dependence on temperature of the emission observed for the MOFs is attractive for potential use in luminescence thermometers.[6] We attribute this rather unusual behavior to the existence of two emitting states, **N*** and **T***, in thermal equilibrium (Scheme 4). **N*** corresponds to a higher lying locally excited state formed after vibrational relaxation of the initially populated Franck−Condon $S_1$ excited state of the bridging ligand, and **T*** corresponds to a lower lying excited state formed after rapid excited state intramolecular proton transfer (ESIPT).[21] The difference in energy between the two emitting states in **AEMOF-3** is estimated from the difference in emission maxima at room temperature and 77 K to be in the region of ca. 1500 $cm^{-1}$. This small energy difference between emitting states has been shown to result in thermally equilibrated luminescence in $[Cu(NN)_2]^+$ (NN = diimine) complexes from both the $^1$MLCT and the $^3$MLCT excited states as thermal population of the upper $^1$MLCT emitting level occurs at room temperature.[22]

**Scheme 4. Schematic Representation of the Two Emitting Forms of the $H_2dhtp^{2-}$ Bridging Ligand**

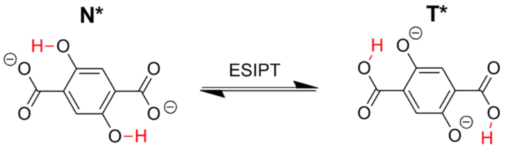

Therefore, in **AEMOF-3**, the room-temperature fluorescence with maximum at 490 nm, as supported by the monoexponential decay it exhibits, is attributed to thermally equilibrated fluorescence predominantly from the **N*** form of the bridging ligand. At 77 K, where thermal excitation is not favored, excitation is largely frozen in the lower lying **T*** state and we thereby observe a bathochromically shifted fluorescence at ca. 527 nm. Detailed calculations on the potential energy surfaces (PES) of the ground state ($S_0$) and the first singlet excited state ($S_1$) of the $H_2dhtp^{2-}$ bridging ligand are in support of the above assignment.[4] The energetics of the ESIPT process have been shown to be extremely sensitive to the polar environment around the emitting chromophore. Comparison of the structures of **AEMOF-2** and **-3** reveals substantial differences in the hydrogen bonding around the hydroxyl groups of the $H_2dhtp^{2-}$ bridging ligand. In **AEMOF-2** the hydroxyl groups are *not* coordinated to $Mg^{2+}$ and are involved exclusively in intramolecular OH···OC H-bonds with the oxygen of the adjacent carboxyl group, whereas in **AEMOF-3** two types of bridging ligand are found: one with uncoordinated hydroxyl groups which form an intramolecular OH···OC H-bond as in the previous case and one with hydroxyl groups coordinated to a $Mg^{2+}$ ion and simultaneously forming an intermolecular OH···$Cl^-$ H-bond involving a close-lying chloride counterion (O − Cl distance 2.945 Å). Presumably, the modest red shift observed in the low-temperature fluorescence spectrum of **AEMOF-2** is a result of structural factors which render the ESIPT process unfavorable. In addition, we cannot rule out the possibility of the red shift in the low-temperature fluorescence spectrum of **AEMOF-3** being due to an intermolecular excited state proton transfer process where the $Cl^-$ counterion acts as proton acceptor since the coordination of the hydroxyl group to a $Mg^{2+}$ center increases its acidity.

Similarly, the room-temperature fluorescence spectrum of **AEMOF-4** is attributed to thermally equilibrated emission predominantly from the **N*** form of the bridging ligand, while the strongly red-shifted emission at 77 K is attributed to the lower lying **T*** form (Scheme 4). The modest red shift observed in the 77 K emission spectrum of **AEMOF-5** in combination with its red-shifted room-temperature emission profile indicates that the contribution of the low-energy **T*** form is far more significant in its thermally equilibrated room-temperature fluorescence. In the case of **AEMOF-6**, its structured room-temperature emission in addition to the different decay constants it shows at different wavelengths points toward dual fluorescence from the closely spaced **N*** and **T*** states with similar radiative lifetimes rather than thermally equilibrated emission. At low temperature, the strong decline of the high-energy feature (ca. 500 nm) in the fluorescence profile of **AEMOF-6** shows that, as in the other **AEMOFs**, excitation is largely frozen in the lower lying emitting state (Figure 9). The bathochromic shift in the room-temperature emission spectra of **AEMOF-5** and **-6** is most probably a result of the ESIPT process being more favorable in the members of the series which contain heavier alkaline earth metal ions ($Sr^{2+}$ and $Ba^{2+}$). A closer look at the site where ESIPT takes place in **AEMOF-4**, **-5**, and **-6** reveals that proton transfer from the hydroxyl group to the adjacent carboxylate oxygen is inhibited by the electrostatic repulsion of the metal center coordinated to the latter (Scheme 5).

**Scheme 5. (A) Representation of the Site where ESIPT Occurs in the AEMOF Series Highlighting the Repulsive Interaction between the Metal Center and the Mobile Proton; (B) Special Case of AEMOF-6 where a $Ba^{2+}$ Ion Is Coordinated to the Hydroxyl Group**

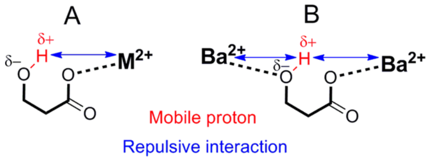

This electrostatic repulsion is expected to be considerably smaller in the case of the heavy alkaline earth metal ions as a result of their greater ionic radius, thus favoring the ESIPT process. Indeed, if we compare the mean carboxylate oxygen to metal distances within the **AEMOF** series we find the expected increasing trend in the order $Mg^{2+}$ (2.047 Å) < $Ca^{2+}$ (2.324 Å) < $Sr^{2+}$ (2.637 Å) < $Ba^{2+}$ (2.940 Å). In the special case of **AEMOF-6**, ESIPT is assisted by the $Ba^{2+}$ ion coordinated to the hydroxyl group of the bridging ligand. This possibly explains the particularly small temperature-induced red shift in the emission profile of **AEMOF-6** in addition to the dual emission, predominantly from the **T*** form, which this compound exhibits at room temperature. It is worth noting that theoretical DFT studies described in the next section, on models of the structural units of the AEMOFs, confirm that the ESIPT process is more favorable in the members of the series which contain heavier alkaline earth metal ions.

Finally, Figure 10 shows the color points of the **AEMOF** series at both room temperature and 77 K. Most notably, the room-temperature emission of **AEMOF-6** is clearly in the yellow region of the spectrum, and **AEMOF-4** shows the most evident color change from turquoise to yellow upon lowering the temperature from 298 to 77 K. Note that the yellow emission of **AEMOF-6** is a property highly desired in light-emitting diodes (LEDs).[7] To the best of our knowledge, only one MOF, namely, the compound $[Ba(Im)_2]$ (Im = imidazole) doped with Eu, showed yellow emission with a quantum yield of 32%.[7] However, the luminescence in this MOF is due to 5d → 4f transitions in the $Eu^{2+}$ ions. Thus, **AEMOF-6** represents the first example of a MOF showing purely ligand-based yellow luminescence with a quantum yield (~34%) exceeding that of the Eu-doped barium imidazolate.

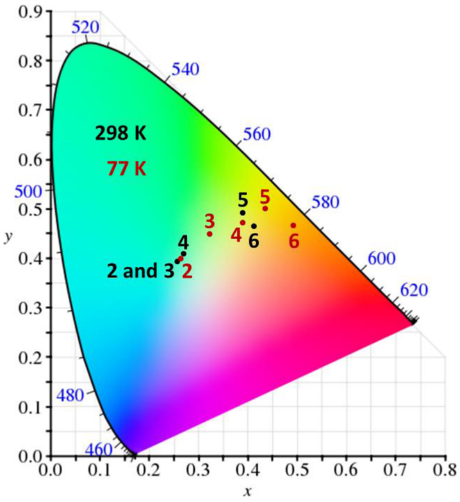

**Figure 10.** CIE chromaticity diagram[23] showing the color coordinates of the **AEMOFs** at both room temperature and 77 K. Note that the room-temperature emission of **AEMOF-6** is clearly in the yellow region of the spectrum.

**Theoretical Studies of the Effect of Alkaline Earth Metal Ions on the Excited State Intramolecular Proton Transfer (ESIPT) Switching.** To probe the effect of the alkaline earth metal ions on the ESIPT process that possibly occurs in the $H_2dhtp^{2-}$ bridging ligand upon excitation of the AEMOFs under study we calculated the potential energy surfaces (PESs) of the ground state ($S_0$) and the lowest energy excited singlet state ($S_1$) of model complexes, **M1**−**4**, along the proton transfer coordinate in the gas phase. The computed PESs along with the calculated excitation and emission transitions and the optimized structures of the $S_0$ and $S_1$ states of the model complexes with selected structural parameters are shown in Figure 11.

Inspection of Figure 11 reveals that the alkaline earth metal ions block the ESIPT process upon excitation to the $S_1$ state of the model complexes in comparison to the free ligand, though to a different extent. Thus, the proton transferred in the $S_1$ state of the model complexes is moved toward the carboxylic oxygen atom by 0.036, 0.053, 0.069, and 0.118 Å in the Mg (**M1**), Ca (**M2**), Sr (**M3**), and Ba (**M4**) model complexes, respectively; the proton transfer increases as the weight of the alkaline earth metal ion increases. The suppression of the ESIPT process in the $S_1$ state of the model complexes results from lessening of the

DOI: 10.1021/acs.inorgchem.5b00539
*Inorg. Chem.* 2015, 54, 5813−5826

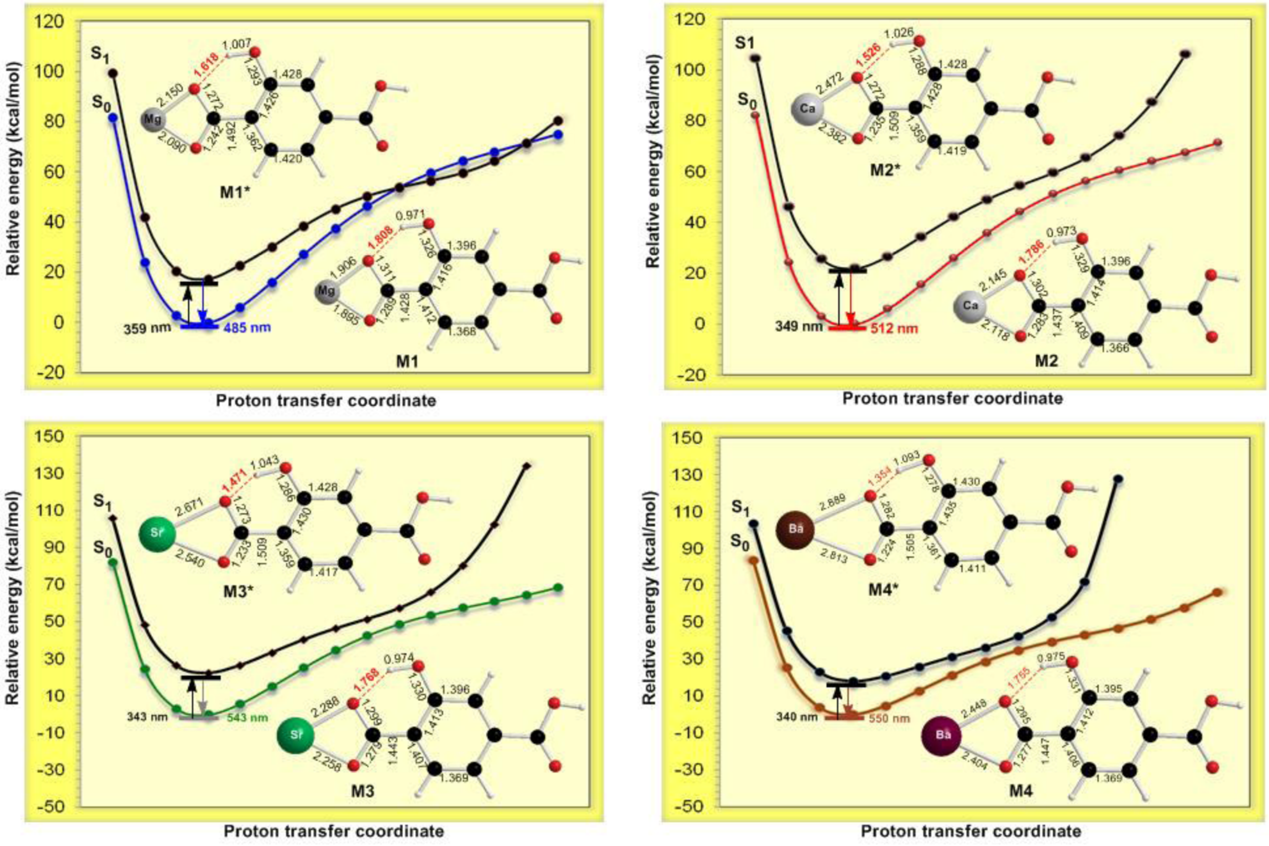

**Figure 11.** Potential energy surfaces of the possible photophysical processes along the proton transfer coordinate in the gas phase calculated at the PBE0/Def2-TZVP level of theory. **M1−4** and **M1−4*** correspond to $S_0$ and $S_1$ states of fluorophore structures located on the GSIPT (ground state intramolecular proton transfer) PES and the lowest energy fluorophore structure located on the ESIPT (excited state intramolecular proton transfer) PES, respectively.

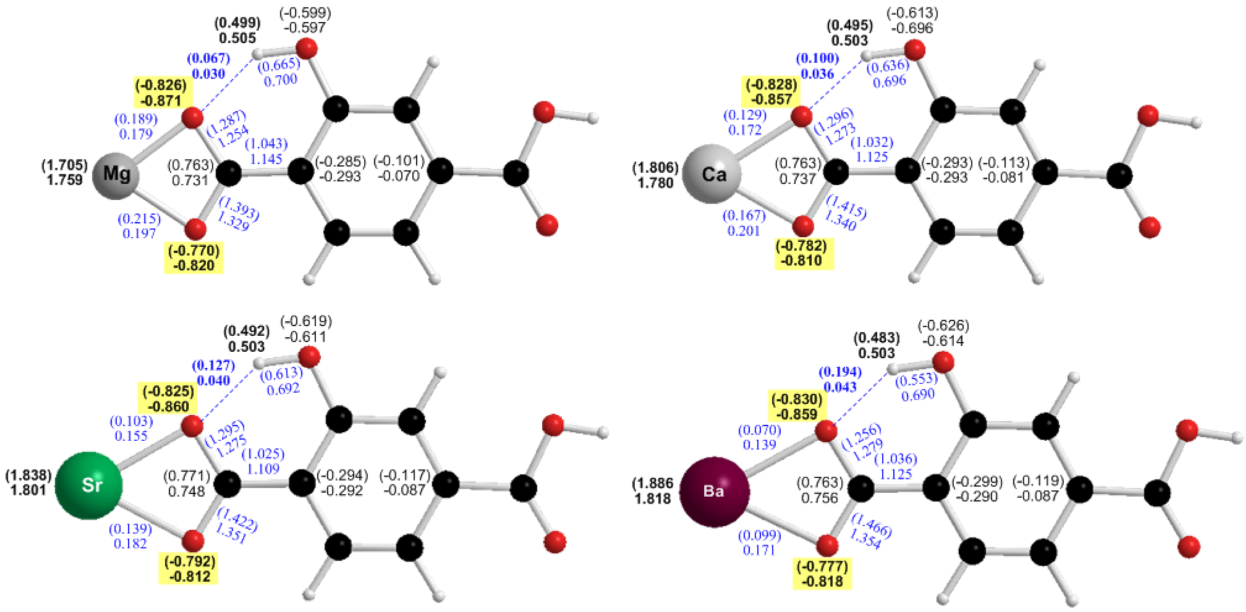

**Figure 12.** Natural atomic charges and the Wiberg bond indices (WBIs) for the $S_0$ and $S_1$ (figures in parentheses) states of the model complexes calculated by the natural bond orbital (NBO) population analysis approach at the PBE0/Def2-TZVP level of theory.

electron density on the carboxylic O atoms of the model 2-hydroxy-terephthalate ligand (htp$^-$) induced by the interaction with the alkaline earth metal ions. Figure 12 shows the natural atomic charges and the Wiberg bond indices (WBIs) for the $S_0$ and $S_1$ states of the model complexes calculated by the natural bond orbital (NBO) population analysis approach.

Perusal of Figure 12 reveals that in all model complexes transfer of electron density from the htp$^-$ ligand to the alkaline earth metal dications occurs in both the ground $S_0$ and the singlet excited $S_1$ states. In the ground $S_0$ states the charge transferred amounts to 0.241, 0.220, 0.199, and 0.182 |e| for the **M1**, **M2**, **M3**, and **M4** model complexes, respectively. The same holds true for the singlet excited $S_1$ states where the charge transferred is 0.295, 0.194, 0.162, and 0.114 |e| for the **M1***, **M2***, **M3***, and **M4*** model complexes, respectively. Notice that in both the $S_0$ and the $S_1$ states of the model complexes the charge transferred follows the trend **M1**(**M1***) > **M2**(**M2***) > **M3**(**M3***) > **M4**(**M4***). The observed charge transfer from the htp$^-$ ligand to the alkaline earth metal dications in the singlet excited $S_1$ states accounts well for the observed moving distances of the proton toward the alkaline earth metal ions.

The optimized geometries of the singlet excited $S_1$ states show significant structural changes with respect to the optimized geometries of the ground $S_0$ states of the model complexes. In the $S_1$ states the M−O distance are elongated by 0.2 up to 0.5 Å relative to the M−O distances in the $S_0$ states, with the elongation increasing as one goes down to the group 2 elements. Comparing the mean carboxylate oxygen to metal distances within the **M1−4** and **M1−4*** series we find the expected increasing trends in the order **M1** (1.901 Å) < **M2** (2.132 Å) < **M3** (2.273 Å) < **M4** (2.426 Å) and **M1*** (2.120 Å) < **M2*** (2.427 Å) < **M3*** (2.606 Å) < **M4*** (2.851 Å) in line with experimental observations. On the other hand, both the C(O)O bonds of the carboxylato moiety and the C−OH bonds are shortened in the $S_1$ states by 0.01−0.05 Å. Remarkable structural changes occur in the benzene ring of the model complexes upon excitation to the $S_1$ states, resulting in the expansion of the ring relative to the benzene ring of the $S_0$ states. These structural changes result from the redistribution of the electron density on the ligand framework induced by the excitation. The interaction of the alkaline earth metal ions with the htp$^-$ ligand exhibits mainly electrostatic character with small contribution of covalent character which decreases going down to group 2 elements (compare the estimated WBIs given in Figure 12). The computed interaction energies of the alkaline earth metal ions with the htp$^-$ ligand in the $S_0$ states are 350, 297, 272, and 254 kcal/mol at the PBE0/Def2-TZVP level for the **M1**, **M2**, **M3**, and **M4** complexes, respectively. Noteworthy, except for the **M1** complex, the weak covalent interactions decrease in the $S_1$ states.

Generally the redistribution of the electron density over the whole framework of the htp$^-$ ligand induced by the alkaline earth metal ions affects the delocalized $\pi$-electron system of the complexes and hence the aromatic character of the benzene ring. This is reflected on the calculated NICS$_{zz}$($R$)-scan curves for the **M1−M4** model complexes, which are given in Figure S25, Supporting Information.

Noteworthy, upon coordination of the htp$^-$ ligand to alkaline earth metal ions the aromaticity of the benzene ring expressed by the minimum NICS$_{zz}$(1.1) values (in ppm) slightly increases along the **M1−M4** series: **M4** (−21.3) < **M3** (−21.1) < **M2** (−20.6) < **M1** (−19.9) < htp$^-$ (−19.5). Interestingly, the **M1−M4** complexes keep the aromaticity in their singlet excited $S_1$ state, slightly increasing with respect to the aromaticity of their ground $S_0$ state, but are lower than the aromaticity of the $S_1$ state of the “free” htp$^-$ ligand: htp$^-$ (−22.9) < **M4** (−21.5) < **M3** (−21.4) < **M2** (−20.9) < **M1** (−20.4). Taking into consideration that the magnitude of the induced diatropic and paratropic ring currents are determined by the excitation energies of the most significant $T_{x,y}$- and $R_z$-allowed occupied → unoccupied and occupied → singly occupied molecular orbital transitions,[24] we calculated the absorption and emission spectra of the **M1−M4** complexes. The calculated $\lambda_{abs}$ and $\lambda_{em}$ along with the NICS$_{zz}$(1.1) values, dipole moments $\mu$, and interaction energies $D_0$ of the model complexes are collected in Table 4.

**Table 4. Calculated $\lambda_{abs}$ and $\lambda_{em}$ along with the NICS$_{zz}$(1.1) Values, Dipole Moments $\mu$, and Interaction Energies $D_0$ of the Model Complexes**

| compound | $\lambda_{abs}$ (nm) | $\lambda_{em}$ (nm) | NICS$_{zz}$(1.1) (ppm) | $\mu$ (Debye) | $D_0$ (kcal mol$^{-1}$) |
|---|---|---|---|---|---|
| **M1** | 359 | 485 | −19.9 | 19.4 | 350 |
| **M2** | 349 | 512 | −20.6 | 20.9 | 297 |
| **M3** | 343 | 543 | −21.1 | 22.9 | 272 |
| **M4** | 340 | 550 | −21.3 | 24.1 | 254 |

It can be seen that the alkaline earth metal ions slightly affect the absorption maxima in the absorption spectra of the **M1−M4** complexes, inducing small blue shifts (3−10 nm) as one goes down to the group 2 elements in line with experiment. Notice that such small blue shifts could not be resolved in the diffuse reflectance spectra of the **AEMOFs** studied due to the very broad absorption bands observed. However, the alkaline earth metal ions significantly affect the emission maxima in the fluorescence spectra of the **M1−M4** complexes, inducing remarkable red shifts (7−31 nm) as the weight of the alkaline earth metal ion increases in good agreement with the experimental data (red shifts of 17−31 nm).

To probe the observed trends in the absorption and fluorescence spectra of the **M1−M4** complexes the absorption and emission bands have thoroughly been analyzed, and assignments of the contributing principal electronic transitions associated with individual excitations have been made. The absorption bands arise from electronic transitions associated with HOMO → LUMO+1 excitations in the $S_0$ states, with HOMO and LUMO+1 being inherently the $\pi$ and $\pi^*$ molecular orbitals (MOs) of the htp$^-$ ligand delocalized mainly on the six-membered carbocyclic ring (Scheme 6).

The relatively small perturbation of the $\pi$ and $\pi^*$ system of the coordinated htp$^-$ ligand account well for the marginal effect of the alkaline earth metal ions on the absorption maxima of the absorption spectra of the **M1−M4** complexes. On the other hand, the emission bands arise from electronic transitions which are ascribed to HOMO−1 ← LUMO, LUMO+3, electronic

**Scheme 6. 3-D Contour Plots of the Molecular Orbitals Associated with the Principal Electronic Transitions in the Absorption and Emission Spectra of M1−M4 Complexes**

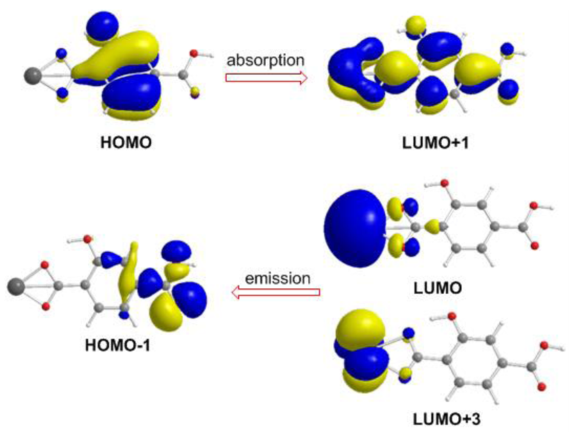

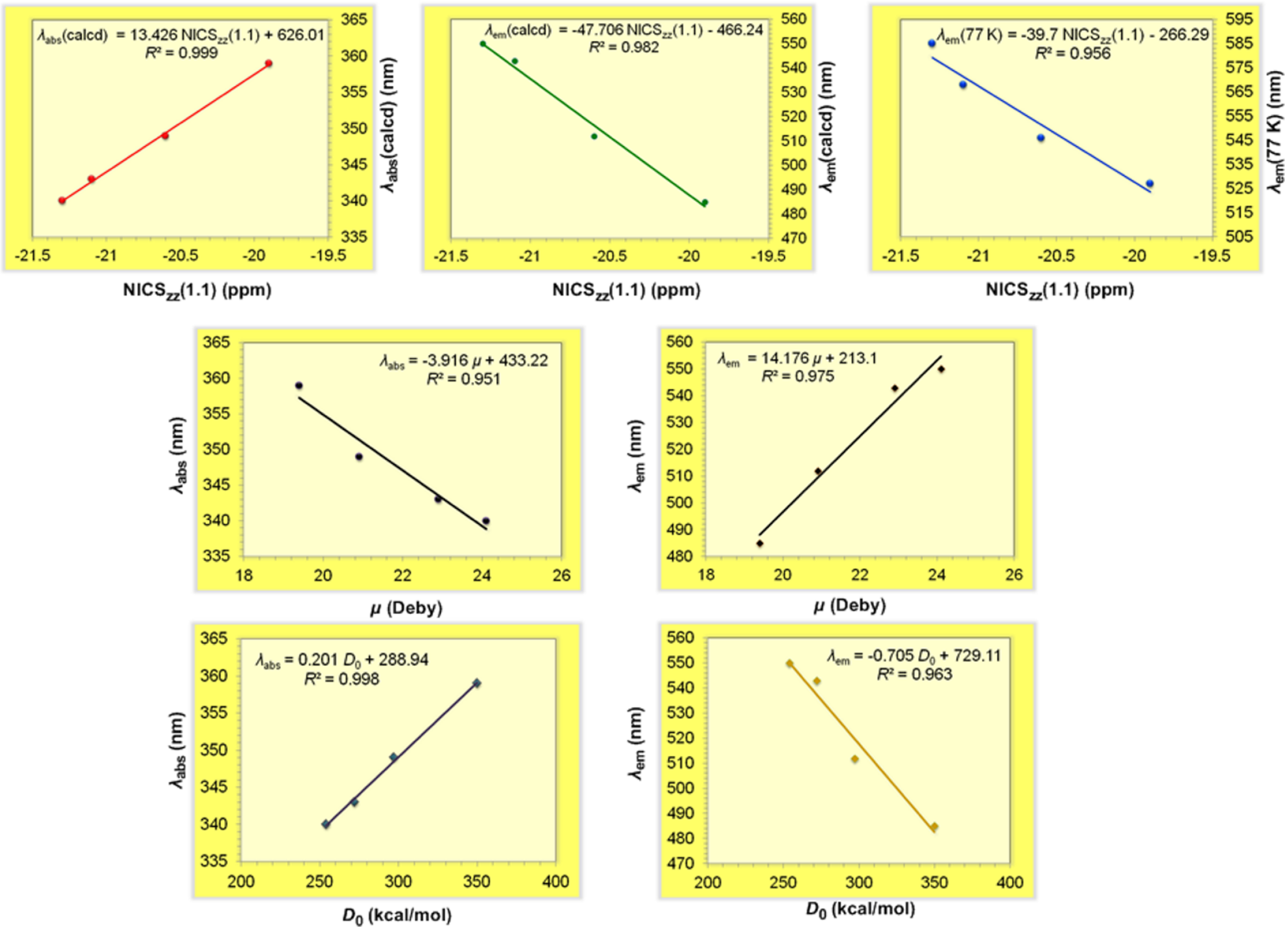

**Figure 13.** Linear correlations of $\lambda_{abs}$ and $\lambda_{em}$ with the NICSzz(1.1) values, dipole moments $\mu$, and dissociation energies $D_0$ calculated at the PBE0/Def2-TZVP level of theory.

transitions in the $S_1$ states (Scheme 6). The HOMO−1 is a $\sigma$-type MO localized mainly on the −C(O)OH carboxylic moiety, while LUMO and LUMO+3 are almost pure *n*s and *n*p AOs of the alkaline earth metal ions. The nature of the electronic transitions occurring in the emission from the $S_1$ states assigned as MLCT (metal-to-ligand) transitions nicely explain the stronger effect of the alkaline earth metal ions on the emission maxima of the fluorescence spectra of the **M1−M4** complexes. Noteworthy, excellent linear correlations of the $\lambda_{abs}$ and $\lambda_{em}$ with the NICSzz(1.1) values, dipole moments $\mu$ (Debye), and dissociation energies $D_0$ (kcal/mol) of the **M1−M4** complexes shown in Figure 13 are obtained, illustrating the effect of the alkaline earth metal ions on the photophysical properties of the **AEMOFs** under study.

## ■ CONCLUSIONS

In conclusion, a series of new alkaline earth metal ion−dihydroxy−terephthalate MOFs (**AEMOF-2−6**) has been isolated. The compounds showed 3-D structures with the exception of **AEMOF-3**, exhibiting a 2-D structure, diverse structural topologies, and a number of unprecedented structural features, such as novel SBUs and unique $H_2dhtp^{2-}$ coordination modes. Clearly, alkaline earth metal ion MOFs represent a relatively unexplored subcategory of metal organic frameworks with a number of interesting characteristics and properties unseen in other type of MOFs. Indeed, compounds **AEMOF-2−6** show bright fluorescence with colors ranging from turquoise to yellow. Detailed spectroscopic studies show that two closely lying excited states are involved in the photophysics of the **AEMOF** series: **N***, which corresponds to a higher lying locally excited state formed after vibrational relaxation of the initially populated Franck−Condon $S_1$ excited state of the bridging ligand, and **T***, corresponding to a lower lying excited state formed after rapid excited state intramolecular proton transfer (ESIPT). At room temperature, **AEMOFs 2−4** exhibit thermally equilibrated emission predominantly from the **N*** state, while in **AEMOF-5** the participation of both the **N*** and the **T*** states is significant as shown by its strongly red-shifted emission profile. **AEMOF-6** shows dual emission from the **N*** and **T*** states as demonstrated from its wavelength-dependent decay dynamics. The significant contribution of the **T*** state in the room-temperature emission of the $Sr^{2+}$- and $Ba^{2+}$-based **AEMOF-5** and **-6** is explained on the basis of the weaker electrostatic interactions between the larger alkaline earth metal ions and the mobile protons of the bridging ligand, which render the ESIPT process more favorable. At 77 K excitation is largely frozen in the lower lying **T*** state, giving rise to red-shifted emission from the **AEMOF** series. The most pronounced temperature-induced shift is seen in the $Ca^{2+}$-based **AEMOF-4**. Theoretical calculations on model $htpM^+$ (M = Mg, Ca, Sr, Ba) complexes employing DFT methods revealed that the alkaline earth metal ions block the ESIPT process upon excitation to the

$S_1$ state to a different extent. Specifically, the proton transfer increases as the weight of the alkaline earth metal ion increases, in line with the experimental investigations. The effect of the alkaline earth metal ions on the photophysical properties of the **AEMOFs** under study is also mirrored on the excellent linear relationsips of $\lambda_{abs}$ and $\lambda_{em}$ with the NICSzz(1.1) values, dipole moments $\mu$, and dissociation energies $D_0$ of the **M1−M4** complexes.

Finally, this work indicates that alkaline earth metal ion MOFs with ESIPT active bridging ligands may be attractive not only for chemical sensing, as previous work on $Mg-H_2dhtp^{2-}$ MOFs revealed, but also for potential applications in luminescence thermometers and solid state lighting. Ongoing efforts are underway to further develop these materials.

## ■ ASSOCIATED CONTENT

### Ⓢ Supporting Information

PXRD, thermal analyses data, gas sorption data, structural figures, FT-IR spectra, and excitation−emission spectra. The Supporting Information is available free of charge on the ACS Publications website at DOI: 10.1021/acs.inorgchem.5b00539.

## ■ AUTHOR INFORMATION

### Corresponding Authors

*E-mail: tlazarides@chem.auth.gr.
*E-mail: emanos@cc.uoi.gr.

### Notes

The authors declare no competing financial interest.

## ■ ACKNOWLEDGMENTS

The National Strategic Reference Framework, Regional Operational Program of Epirus 2007-2013 (2011/S 29-048013), is acknowledged for supporting the purchase of a PerkinElmer LS55 fluorimeter by the Department of Chemistry of the University of Ioannina. Financial support from the National Science Foundation (Grant DMR-1410169) (M.G.K.) is gratefully acknowledged. The variable-temperature diffraction measurements were carried out in the J. B. Cohen X-ray Diffraction Facility supported by the MRSEC program of the National Science Foundation (DMR-1121262) at the Materials Research Center of Northwestern University. A.B. thanks CNR (PM.P04.010, MACOL, and PB.P04.007.003, N-Chem), ESF-EUROCORES (Project SOLARFUELTANDEM) for funding, and Mr. G. Longino (CNR-ISOF) for technical assistance in the customization of the photophysical setup.

## ■ REFERENCES

(1) (a) Eddaoudi, M.; Moler, D. B.; Li, H. L.; Chen, B. L.; Reineke, T. M.; O'Keeffe, M.; Yaghi, O. M. *Acc. Chem. Res.* **2001**, *34*, 319−330. (b) Ferey, G. *Chem. Soc. Rev.* **2008**, *37*, 191−214.

(2) (a) Zheng, S. T.; Wu, T.; Zhang, J. A.; Chow, M.; Nieto, R. A.; Feng, P. Y.; Bu, X. H. *Angew. Chem., Int. Ed.* **2010**, *49*, 5362−5366. (b) Farha, O. K.; Yazaydin, A. O.; Eryazici, I.; Malliakas, C. D.; Hauser, B. G.; Kanatzidis, M. G.; Nguyen, S. T.; Snurr, R. Q.; Hupp, J. T. *Nat. Chem.* **2010**, *2*, 944−948. (c) Xue, D. X.; Cairns, A. J.; Belmabkhout, Y.; Wojtas, L.; Liu, Y.; Alkordi, M. H.; Eddaoudi, M. *J. Am. Chem. Soc.* **2013**, *135*, 7660−7667. (d) Morris, R. E.; Wheatley, P. S. *Angew. Chem., Int. Ed.* **2008**, *47*, 4966−4981. (e) Horike, S.; Shimomura, S.; Kitagawa, S. *Nat. Chem.* **2009**, *1*, 695−704. (f) Neofotistou, E.; Malliakas, C. D.; Trikalitis, P. N. *Chem.—Eur. J.* **2009**, *15*, 4523−4527. (g) Ma, L. Q.; Falkowski, J. M.; Abney, C.; Lin, W. B. *Nat.Chem.* **2010**, *2*, 838−846. (h) Wei, Z.; Gu, Z.-Y.; Arvapally, R.; Chen, Y.-P.; McDougald, R.; Yakovenko, A.; Feng, D.; Omary, M.; Zhou, H.-C. *J. Am. Chem. Soc.* **2014**, *136*, 8269−8276.

(3) (a) Wang, L. J.; Deng, H.; Furukawa, H.; Gándara, F.; Cordova, K. E.; Peri, D.; Yaghi, O. M. *Inorg. Chem.* **2014**, *53*, 5881−5883. (b) Caskey, S. R.; Wong-Foy, A. G.; Matzger, A. J. *J. Am. Chem. Soc.* **2008**, *130*, 10870−10871. (c) Zhou, W.; Wu, H.; Yildirim, T. *J. Am. Chem. Soc.* **2008**, *130*, 15268−15269. (d) Han, L.; Qin, L.; Xu, L.; Zhou, Y.; Sunb, J.; Zou, X. *Chem. Commun.* **2013**, *49*, 406−408. (e) Dietzel, P. D. C.; Blom, R.; Fjellvåg, H. *Eur. J. Inorg. Chem.* **2008**, *23*, 3624−3632. (f) Shustova, N. B.; Cozzolino, A. F.; Reineke, S.; Baldo, M.; Dinca, M. *J. Am. Chem. Soc.* **2013**, *135*, 13326−13329. (g) K. Jayaramulu, K.; Kanoo, P.; George, S. J.; Maji, T. K. *Chem. Commun.* **2010**, *46*, 7906−7908. (h) Jayaramulu, K.; Narayanan, R. P.; George, S. J.; Maji, T. K. *Inorg. Chem.* **2012**, *51*, 10089−10091. (i) Mallick, A.; Garai, B.; Addicoat, M. A.; Petkov, P. St.; Heine, T.; Banerjee, R. *Chem. Sci.* **2015**, *6*, 1420−1425.

(4) Douvali, A.; Tsipis, A. C.; Eliseeva, S. V.; Petoud, S.; Papaefstathiou, G. S.; Malliakas, C. D.; Papadas, I.; Armatas, G. S.; Margiolaki, I.; Kanatzidis, M. G.; Lazarides, T.; Manos, M. J. *Angew. Chem., Int. Ed.* **2015**, *54*, 1651−1656.

(5) (a) Wu, J.; Liu, W.; Ge, J.; Zhang, H.; Wang, P. *Chem. Soc. Rev.* **2011**, *40*, 3483−3495. (b) Suzuki, N.; Fukazawa, A.; Nagura, K.; Saito, S.; Nishioka, H. K-.; Yokogawa, D.; Irle, S.; Yamaguchi, S. *Angew. Chem., Int. Ed.* **2014**, *53*, 8231−8235. (c) Kenfack, C. A.; Klymchenko, A. S.; Duportail, G.; Burger, A.; Mély, Y. *Phys. Chem. Chem. Phys.* **2012**, *14*, 8910−8918. (d) Zhao, J.; Ji, S.; Chen, Y.; Huimin Guo, H.; Yang, P. *Phys. Chem. Chem. Phys.* **2012**, *14*, 8803−8817. (e) Porel, M.; Ramalingam, V.; Domaradzki, M. E.; Young, V. G., Jr.; Ramamurthya, V.; Muthyala, R. S. *Chem. Commun.* **2013**, *49*, 1633−1635. (f) Goswami, S.; Manna, A.; Paul, S.; Das, A. K.; Aich, K.; Nandi, P. K. *Chem. Commun.* **2013**, *49*, 2912−2914. (g) Kanoo, P.; Ghosh, A. C.; Cyriac, S. T.; Maji, T. K. *Chem.—Eur. J.* **2012**, *18*, 237−244.

(6) (a) Kreno, L. E.; Leong, K.; Farha, O. K.; Allendorf, M.; Van Duyne, R. P.; Hupp, J. T. *Chem. Rev.* **2012**, *112*, 1105−1125. (b) Takashima, Y.; Martínez, V. M.; Furukawa, S.; Kondo, M.; Shimomura, S.; Uehara, H.; Nakahama, M.; Sugimoto, K.; Kitagawa, S. *Nat. Commun.* **2011**, *2*, 168. (c) Liu, D.; Lu, K.; Poon, C.; Lin, W. *Inorg. Chem.* **2014**, *53*, 1916−1924. (d) Chen, B.; Wang, L.; Xiao, Y.; Fronczek, F. R.; Xue, M.; Cui, Y.; Qian, G. *Angew. Chem., Int. Ed.* **2009**, *48*, 500−503. (e) Harbuzaru, B. V.; Corma, A.; Rey, F.; Atienzar, P.; Jorda, J. L.; Garcia, H.; Ananias, D.; Carlos, L. D.; Rocha, J. *Angew. Chem., Int. Ed.* **2008**, *47*, 1080−1083. (f) Hu, Z.; Deibert, B. J.; Li, J. *Chem. Soc. Rev.* **2014**, *43*, 5815−5840.

(7) Rybak, J.-C.; Hailmann, M.; Matthes, P. R.; Zurawski, A.; Nitsch, J.; Steffen, A.; Heck, J. G.; Feldmann, C.; Götzendörfer, S.; Meinhardt, J.; Sextl, G.; Kohlmann, H.; Sedlmaier, S. J.; Schnick, W.; Buschbaum, K. M-. *J. Am. Chem. Soc.* **2013**, *135*, 6896−6902.

(8) (a) Bruker. *Apex2*, Version 2; Bruker AXS Inc.: Madison, WI, 2006. (b) Sheldrick, G. M. *SHELXTL*, 5.1 ed.; Bruker-AXS: Madison, WI, 1998.

(9) (a) Barbieri, A.; Accorsi, G. *EPA Newslett.* **2006**, 26−35. (b) Aurisicchio, C.; Ventura, B.; Bonifazi, D.; Barbieri, A. *J. Phys. Chem. C* **2009**, *113*, 17927−17935.

(10) Frisch, M. J. et al. *Gaussian 09*, Revision B.01; Gaussian, Inc.: Wallingford, CT, 2010. See the Supporting Information for the full reference.

(11) (a) Ernzerhof, M.; Scuseria, G. E. *J. Chem. Phys.* **1999**, *110*, 5029. (b) Adamo, C.; Barone, V. *Chem. Phys. Lett.* **1997**, *274*, 242. (c) Adamo, C.; Barone, V. *J. Chem. Phys.* **1999**, *110*, 6160. (d) Adamo, C.; Scuseria, G. E.; Barone, V. *J. Chem. Phys.* **1999**, *111*, 2889. (e) Adamo, C.; Barone, V. *Theor. Chem. Acc.* **2000**, *105*, 169. (f) Veter, V.; Adamo, C.; Maldivi, P. *Chem. Phys. Lett.* **2000**, *325*, 99.

(12) (a) Kaupp, M.; Schleyer, P. V.; Stoll, H.; Preuss, H. *J. Chem. Phys.* **1991**, *94*, 1360−1366. (b) Lim, I. S.; Stoll, H.; Schwerdtfeger, P. *J. Chem. Phys.* **2006**, *124*, 034107. (c) EMSL basis set exchange, https://bse.pnl.gov/bse/portal, accessed Aug 11, 2014.

(13) (a) Reed, A. E.; Curtiss, L. A.; Weinhold, F. *Chem. Rev.* **1988**, *88*, 899. (b) Weinhold, F. In *The Encyclopedia of Computational Chemistry*; Schleyer, P. v. R., Ed.; Wiley: Chichester, U.K., 1998; p 1792. (c) Glendening, E. D.; Badenhoop, J. K.; Reed, A. E.; Carpenter, J. E.; Bohmann, J. A.; Morales, C. M.; Landis, C. R.; Weinhold, F. *NBO 6.0*;

Theoretical Chemistry Institute, University of Wisconsin: Madison, 2013.

(14) (a) Ditchfield, R. *Mol. Phys.* **1974**, *27*, 789. (b) Gauss, J. *J. Chem. Phys.* **1993**, *99*, 3629.

(15) Schleyer, P. v. R.; Maerker, C.; Dransfeld, A.; Jiao, H.; Hommes, N. J. *J. Am. Chem. Soc.* **1996**, *118*, 6317.

(16) Macrae, C. F.; Edgington, P. R.; McCabe, P.; Pidcock, E.; Shields, G. P.; Taylor, R.; Towler, M.; van De Streek, J. *J. Appl. Crystallogr.* **2006**, *39*, 453−457.

(17) O'Keeffe, M.; Yaghi, O. M. *Chem. Rev.* **2012**, *112*, 675−702.

(18) Cheansirisomboon, A.; Uber, J. S.-; Massera, C.; Roubeau, O.; Youngme, S.; Gamez, P. *Eur. J. Inorg. Chem.* **2014**, *26*, 4385−4393.

(19) Liang, P.-C.; Liu, H.-K.; Yeh, C.-T.; Lin, C.-H.; Zima, V. *Cryst. Growth Des.* **2011**, *11*, 699−708.

(20) Dietzel, P. D. C.; Blom, R.; Fjellvåg, H. *Z. Anorg. Allg. Chem.* **2009**, *635*, 1953−1958.

(21) (a) Lakowicz, J. R. *Principles of Fluorescence Spectroscopy*, 3rd ed.; Springer, New York, 2006. (b) Agmon, N. *J. Phys. Chem. A* **2005**, *109*, 13−35. (c) Schneider, S. *J. Phys. Chem. A* **2000**, *104*, 5898−5909.

(22) (a) Kirchhoff, J. R.; Gamache, R. E.; Blaskie, M. W.; Del Paggio, A. A.; Lengel, R. K.; McMillin, D. R. *Inorg. Chem.* **1983**, *22*, 2380−2384. (b) Felder, D.; Nierengarten, J.-F.; Barigelletti, F.; Ventura, B.; Armaroli, N. *J. Am. Chem. Soc.* **2001**, *123*, 6291−6299.

(23) In *Phosphor Handbook*; Shionoya, S., Yen, W. M., Eds.; CRC Press: Boca Raton, FL, 1999.

(24) (a) Lazzeretti, P.; Malagoli, M.; Zanasi, R. *Chem. Phys. Lett.* **1994**, *220*, 299−304. (b) Coriani, S.; Lazzeretti, P.; Malagoli, M.; Zanasi, R. *Theor. Chim. Acta* **1994**, *89*, 181−192. (c) Lazzeretti, P. In *Progress in Nuclear Magnetic Resonance Spectroscopy*; Emsley, J. W., Feeney, J., Sutcliffe, L. H., Eds.; Elsevier: Amsterdam, The Netherlands, 2000; Vol. *36*, p 1. (d) Steiner, E.; Fowler, P. W. *Chem. Commun.* **2001**, 2220−221. (e) Steiner, E.; Fowler, P. W. *J. Phys. Chem. A* **2001**, *105*, 9553−9562. (f) Fowler, P. W.; Steiner, E.; Havenith, R. W. A.; Jenneskens, L. W. *Magn. Reson. Chem.* **2004**, *42*, S68−S78. (g) Corminboeuf, C.; King, R. B.; Schleyer, P. v. R. *ChemPhysChem* **2007**, *8*, 391−398.